nature communications

Article

https://doi.org/10.1038/s41467-025-57964-7

Smart gel polymer electrolytes enlightening high safety and long life sodium ion batteries

Received: 21 July 2024

Accepted: 9 March 2025

Published online: 26 March 2025

Check for updates

Li Du[1,2,3,4], Gaojie Xu[1,2,3] ✉, Chenghao Sun[1,2,3], Yu-Han Zhang[1,2,3], Huanrui Zhang[1,2,3] ✉, Tiantian Dong[1,2,3] ✉, Lang Huang[1,2,3], Jun Ma[1,2,3], Fu Sun[1,2,3], Chuanchuan Li[1,2,3], Xiangchun Zhuang[1,2,3], Shenghang Zhang[1,2,3], Jiedong Li[1,2,3], Bin Xie[1,2,3], Jinzhi Wang[1,2,3], Jingwen Zhao[1,2,3], Jiangwei Ju[1,2,3], Zhiwei Hu[5], Fan-Hsiu Chang[6], Chang-Yang Kuo[6,7], Chien-Te Chen[7], André Hilger[8], Ingo Manke[8], Shanmu Dong[1,2,3] & Guanglei Cui[1,2,3] ✉

The overall performance of sodium-ion batteries, particularly regarding safety and cycle life, remains below expectations due to severe degradation of electrode materials and the electrode/electrolyte interphase. Herein, we develop a smart gel polymer electrolyte for hard carbon||$NaNi_{1/3}Fe_{1/3}Mn_{1/3}O_2$ batteries through the in situ radical polymerization of a cyanoethylurea-containing methacrylate monomer and an isocyanate-based methacrylate monomer in conventional $NaPF_6$-carbonate-based electrolytes. We demonstrate that the smart gel polymer electrolyte facilitates the formation of robust electrode/electrolyte interphase layers, thus improving the thermal and chem-electrochemical stability of the electrodes. When the temperature exceeds 120 °C, the in situ formed gel polymer electrolyte undergoes further cross-linking through nucleophilic addition reactions between urea and isocyanate motifs. This additional crosslinking blocks ion transportation and inhibits crosstalk effects, thus boosting the safety of pouch-type hard carbon||$NaNi_{1/3}Fe_{1/3}Mn_{1/3}O_2$ batteries. Moreover, the smart gel polymer electrolyte enables hard carbon||$NaNi_{1/3}Fe_{1/3}Mn_{1/3}O_2$ full cells to achieve improved cycle life even at the elevated temperature of 50 °C. The design philosophy behind the development of in situ formed smart gel polymer electrolytes offers valuable guidance for creating high-safety, long-life, and sustainable sodium-ion batteries.

Amid the scarcity and considerable price fluctuations of lithium resources, the large-scale commercial advancement of sustainable sodium-ion batteries (SIBs) is accelerating at a rapid rate, owing to their advantages such as cost-effectiveness and the abundance of sodium (Na) resources[1–9]. As one of the most competitive technical routes, SIBs utilizing layered O3-type (ABCABC oxide ion stacking) sodiated transition metal oxide positive electrodes (O3-Na_xTMO_2), hard carbon (HC) negative electrodes, and conventional $NaPF_6$-

[1]Qingdao Industrial Energy Storage Research Institute, Qingdao Institute of Bioenergy and Bioprocess Technology, Chinese Academy of Sciences, Qingdao 266101, China. [2]Shandong Energy Institute, Qingdao 266101, China. [3]Qingdao New Energy Shandong Laboratory, Qingdao 266101, China. [4]College of Electrical Engineering and Automation, Shandong University of Science and Technology, Qingdao 266590, China. [5]Max Planck Institute for Chemical Physics of Solids, Dresden 01187, Germany. [6]National Synchrotron Radiation Research Center, Hsinchu 30076, Taiwan. [7]Department of Electrophysics, National Yang Ming Chiao Tung University, Hsinchu 30010, Taiwan. [8]Helmholtz-Zentrum Berlin für Materialien und Energie, Hahn-Meitner-Platz 1, 14109 Berlin, Germany. ✉e-mail: xugj@qibebt.ac.cn; zhanghr@qibebt.ac.cn; dongtt@qibebt.ac.cn; cuigl@qibebt.ac.cn

carbonate-based electrolytes demonstrate great potential for large-scale commercial applications[10–13]. Nevertheless, the reported overall performance of HC||O3-Na_xTMO_2 batteries, particularly in terms of cycle life and storage life, falls below expectations, especially at elevated temperatures (Supplementary Table 1). Moreover, HC||O3-Na_xTMO_2 SIBs are prone to severe thermal runaway under extreme abuse conditions. Despite this risk, safety evaluations of SIBs have received scant attention thus far[14–18]. The unsatisfactory safety and cycle performance of HC||O3-Na_xTMO_2 batteries are typically attributed to the severe degradation of electrode materials and the electrode/electrolyte interphase, especially under abuse temperature conditions.

The main challenges faced by O3-Na_xTMO_2 positive electrodes include deleterious phase transitions, dissolution of transition metal ions (TMs), mechanical microcracking failure, severe electrolyte oxidation, and oxygen release during thermal runaway processes[10–12,19]. Regarding the HC negative electrode, the representative species of the solid electrolyte interphase (SEI) layer, such as NaF and Na_2CO_3, exhibit high solubility in conventional $NaPF_6$-carbonate-based electrolytes[20–23]. Thus, the SEI layer on the HC negative electrode is easily compromised, leading to continuous electrolyte consumption, loss of active sodium, and gas evolution in SIBs, especially at elevated temperatures. In addition, the dissolution of the SEI layer directly exposes the sodiated HC to the electrolytes, accelerating early-stage self-heating and contributing to thermal runaway in SIBs under abuse conditions[24–27]. In addition, due to the poor chemical, electrochemical, and thermal compatibility of $NaPF_6$-carbonate-based electrolytes with metallic Na[28–30], the presence of quasi-metallic Na clusters in the closed pores of the HC negative electrode[6,31–35] and the easy formation of mossy or dendritic Na on the HC negative electrode during cycling[36,37] will inevitably reduce the safety and cycle life of SIBs. It is noted that these issues have resulted in the commercial development of SIBs lagging behind that of lithium-ion batteries (LIBs), despite SIBs being developed earlier than LIBs. Hence, addressing the safety and longevity issues of HC||O3-Na_xTMO_2 SIBs represent a challenge to both academia and industry.

Recently, the development of in situ formed gel polymer electrolytes with properties such as high flexibility, leak-proofing, interfacial compatibility, high ionic conductivity, large-scale processability, and intrinsic safety has been considered one of the most important strategies for simultaneously enhancing the safety and cycle life of batteries[38–51]. In addition, in situ formed gel polymer electrolytes can effectively mitigate the dissolution or diffusion of certain species, such as TMs, soluble species from the electrode/electrolyte interface, and thermally induced gas species[42]. It is noteworthy that some delicately designed gel polymer electrolytes exhibit the smart capability to undergo additional polymerization or cross-linking under thermal abuse conditions. This property blocks ion transportation and inhibits thermally induced cross-talk effects, thereby enhancing battery safety[52–54]. Therefore, to address the aforementioned safety and longevity challenges of HC||O3-Na_xTMO_2 SIBs and advance their large-scale commercial applications, it is essential to employ the concept of in situ polymerization to design smart gel polymer electrolytes. However, there is currently no existing precedent for developing in situ formed smart gel polymer electrolytes in SIBs, which have distinct battery chemistries and electrolyte chemistries compared to LIBs.

In this study, we innovatively develop a smart gel polymer electrolyte (abbreviated as PCIE) within an HC||O3-$NaNi_{1/3}Fe_{1/3}Mn_{1/3}O_2$ (NFM) battery. This is achieved via thermally-induced in situ radical polymerization of a cyanoethylurea-containing methacrylate (CM) monomer and an isocyanate-based methacrylate (IM) monomer in conventional $NaPF_6$-carbonate-based electrolytes. This represents the instance of utilizing in situ polymerization to design smart gel polymer electrolytes for the performance enhancement of practical HC||O3-Na_xTMO_2 SIBs. The as-constructed in situ PCIE, featuring functional motifs such as cyano, isocyano, and urea, can facilitate the formation of robust electrode/electrolyte interphase layers. This enhances the thermal and chem-electrochemical stability of the electrodes while preventing the generation of gas byproducts, particularly at elevated temperatures. Inspiringly, accelerated rate calorimetry (ARC) demonstrates that the in situ PCIE enhances the safety of pouch-type HC||NFM batteries. This is evidenced by an increased heat-releasing onset temperature (T_{onset}, from 80 °C to 103.6 °C) and thermal runaway onset temperature (T_{tr}, defined as the temperature point when SHR reaches 1 °C min^{-1}, from 137.2 °C to 177.4 °C). When the temperature exceeds 120 °C, the in situ PCIE undergoes further cross-linking via nucleophilic addition reactions between urea and isocyanate. This process blocks ion transportation and inhibits crosstalk effects from thermally-induced gas species, thereby exhibiting a smart thermal response that enhances battery safety. Moreover, the smart gel polymer electrolyte enables practical HC||NFM full cells (positive electrode mass loading of 14 mg cm^{-2}) to achieve improved cycle life, maintaining 80% capacity after 500 cycles even at an elevated temperature of 50 °C.

Results and discussion

Design and preparation of smart in situ PCIE within SIBs

The smart in situ formed PCIE is designed and prepared based on the following principles: (1) The CM monomer, containing both cyano and urea functional motifs, is synthesized through a simple nucleophilic addition of aminoacetonitrile to the low-cost IM monomer (Supplementary Figs. 1, 2, Supplementary Note 1, and Eq. 1). (2) Due to their unsaturated C=C bonds, the CM monomer and IM cross-linker monomer can co-polymerize in conventional $NaPF_6$-carbonate-based electrolytes to form the in situ PCIE directly within SIBs at a moderately high temperature of 60 °C. (3) The nucleophilic addition reaction between urea units and isocyanate groups occurs at temperatures ≥120 °C, blocking ion transportation and inhibiting crosstalk effects from thermally-induced gas species. This imparts smart thermal-responsive characteristics that enhance the safety of SIBs. (4) The developed polymer matrix (PM), rich in cyano, urea, and isocyanate groups, is expected to participate in the formation of robust electrode/electrolyte interphase layers. This is conducive to enhancing the thermal and chem-electrochemical stability of the electrodes and preventing the generation of gas byproducts, especially at elevated temperatures. The structures of the CM monomer, IM monomer, smart in situ PCIE, and cross-linked PCIE are depicted (the first row of Fig. 1a–c). The two monomers, CM and IM, are dissolved into the conventional liquid $NaPF_6$-carbonate-based electrolyte, which is then injected into the HC||NFM full cells. The assembled HC||NFM full cells are then heated to 60 °C to facilitate the co-polymerization of the two monomers. As shown in Supplementary Figs. 3, 4, the liquid electrolyte containing the monomers transforms into a transparent, immobilized gel after the thermally induced polymerization process (Supplementary Note 2). The successful co-polymerization of CM and IM monomers at 60 °C is verified by Fourier transform infrared (FTIR) spectroscopy analysis. The characteristic peak of the unsaturated C=C bonds at around 1634 cm^{-1} disappears after the thermally-induced polymerization process (the second row of Fig. 1a, b). The number-average molecular weight (M_n) of the PM in PCIE is about 2.9×10^5 Da (Supplementary Figs. 5, 6 and Supplementary Note 3). Na^+ transference numbers, linear sweep voltammetry (LSV), and ionic conductivity of the as-developed electrolytes with varied LE uptakes were measured in Supplementary Figs. 7–9, Supplementary Note 4, and Supplementary Table 2. Encouragingly, the ionic conductivity of the optimized in situ PCIE reaches 2.3 mS cm^{-1} at 30 °C, which is sufficient to meet the requirements for the normal operation of sustainable SIBs (Supplementary Fig. 9). More importantly, the in situ PCIE contains a large number of functional groups (e.g., −CN, −NCO, and urea), which are advantageous for forming robust positive electrode electrolyte interphase (CEI) and SEI layers[53].

https://doi.org/10.1038/s41467-025-57964-7

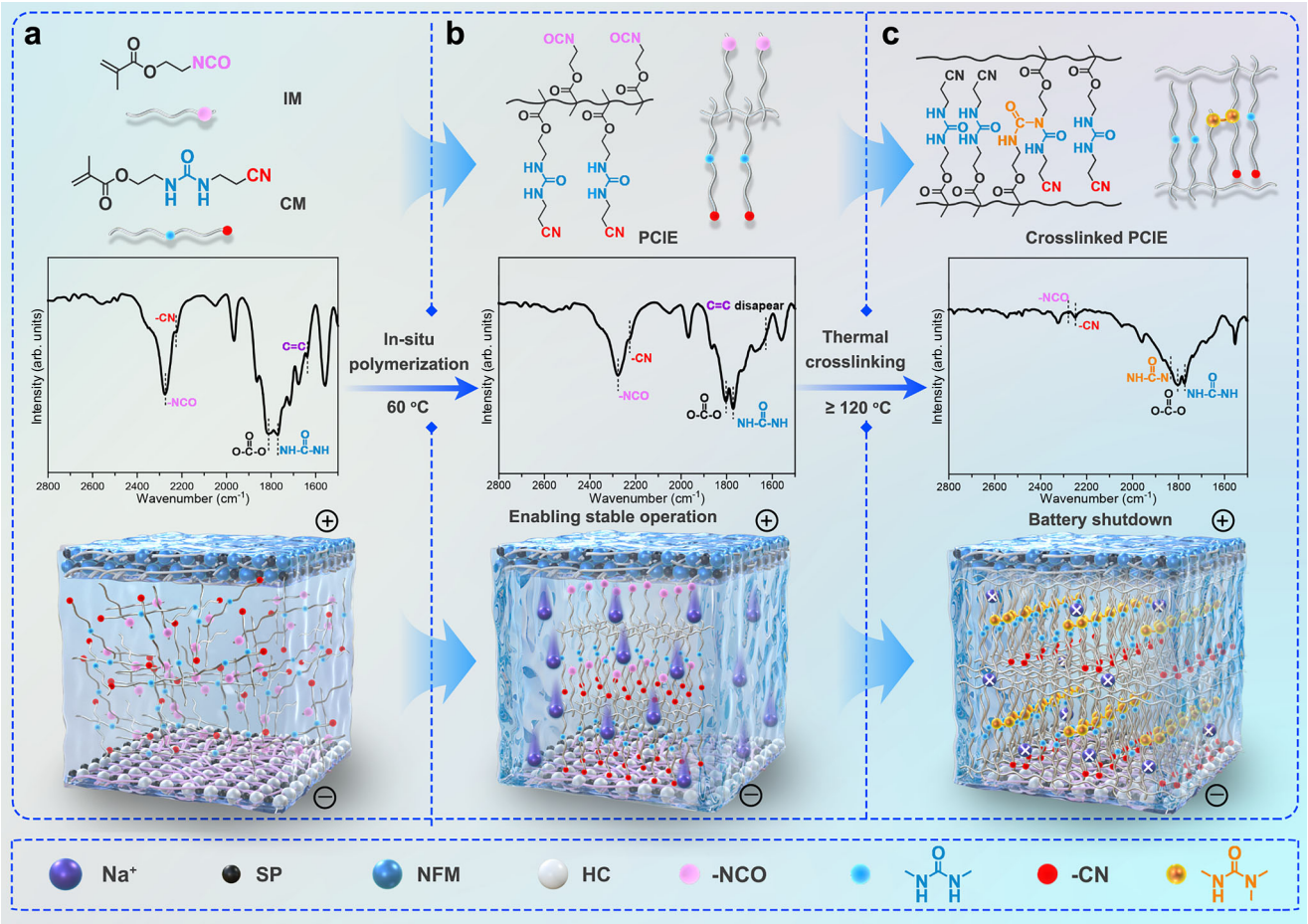

Fig. 1 | Schematic illustration of in situ formed smart gel polymer electrolyte. **a** Monomers in liquid electrolytes at room temperature. **b** In situ formed gel polymer electrolyte (PCIE) obtained at 60 °C. **c** The further cross-linked gel polymer electrolyte (Cross-linked PCIE) at temperatures exceeding 120 °C. The first row is the structures of monomers and polymers. The second row is the FTIR spectra of varied electrolytes. The third row is the schematic illustration of varied electrolytes within HC||NFM full cells.

It is also noted that the dissolution of SEI components (such as NaF and Na_2CO_3) into carbonate solvents can be alleviated because some free carbonate solvents are immobilized by the PM[47]. On the other hand, when the temperature exceeds 120 °C, the in situ PCIE exhibits a smart thermal response by undergoing cross-linking (Fig. 1c). After thermal treatment at 120 °C, the −NCO peaks at 2278 cm^{-1} become weaker, and a carbonyl unit peak at 1844 cm^{-1}, corresponding to −HNCO−N−, forms. This confirms that cross-linking reactions between the urea and isocyanate functional motifs have occurred (the second row of Fig. 1b, c, Supplementary Fig. 10, and Supplementary Note 5). Compared with PCIE, the cross-linked PCIE exhibits a much higher glass transition temperature (T_g) and a decreased free volume value of polymer segments, therefore showing a reduced Na^+ conduction ability and thus enabling battery thermal shutdown (Supplementary Figs. 11 and 12, and Supplementary Note 6). It is anticipated that the cross-linked in situ PCIE will help to cut down Na^+ transportation and crosstalk effects from thermally induced gas species during thermal runaway processes (the third row of Fig. 1b, c), thereby delaying the onset temperature of battery thermal runaway. Therefore, the developed smart in situ PCIE is expected to ensure high safety and long life for HC||NFM SIBs.

Safety enhancement of HC||NFM SIBs by smart in situ PCIE

ARC in heat-wait-search (HWS) mode is employed to investigate the thermal characteristics of HC||NFM pouch cells using the smart in situ PCIE. It is well known that in ARC testing, increased critical temperatures, such as the T_{onset} and T_{tr}, along with a decreased self-heating rate after the thermal runaway, indicate high thermal safety for the battery[41]. As shown in Fig. 2a, the T_{onset} and T_{tr} of 100% SOC (state of charge) HC||NFM pouch cells using smart in situ PCIE is 103.6 and 177.4 °C, respectively. In sharp contrast, T_{onset} and T_{tr} for the control cells using LE is 80.0 °C and 137.2 °C, respectively. Thus, for smart in situ PCIE, the T_{onset} and T_{tr} are increased by 23.6 °C and 40.2 °C, respectively. Moreover, the self-heating rate (SHR) during the battery thermal runaway process is also reduced by smart in situ PCIE (insets of Fig. 2a). Similar to LIBs, the thermal runaway process in SIBs involves multiple sources of heat, including SEI decomposition, reactions between electrodes and electrolyte, short-circuiting of electrodes, electrolyte decomposition, and combustion. These factors cause chain reactions that release heat, each triggering additional thermal events. Thus, it is difficult to quantitatively distinguish the heat contribution of each factor during the thermal runaway chain reactions[55,56].

To uncover the underlying mechanisms by which the smart in situ PCIE enhances the thermal safety of HC||NFM pouch cells, the thermal stability of a fully desodiated NFM positive electrode and a fully sodiated HC negative electrode is tested by ARC and differential scanning calorimetry (DSC). It is revealed that the as-developed smart in situ PCIE provides both the fully desodiated NFM positive electrode and the fully sodiated HC negative electrode with higher thermal stability and lower total heat release. Specifically, with the assistance of the smart in situ PCIE, the T_{onset} and T_{tr} of the fully desodiated NFM positive electrodes are increased by 25 °C and 9 °C, respectively

https://doi.org/10.1038/s41467-025-57964-7

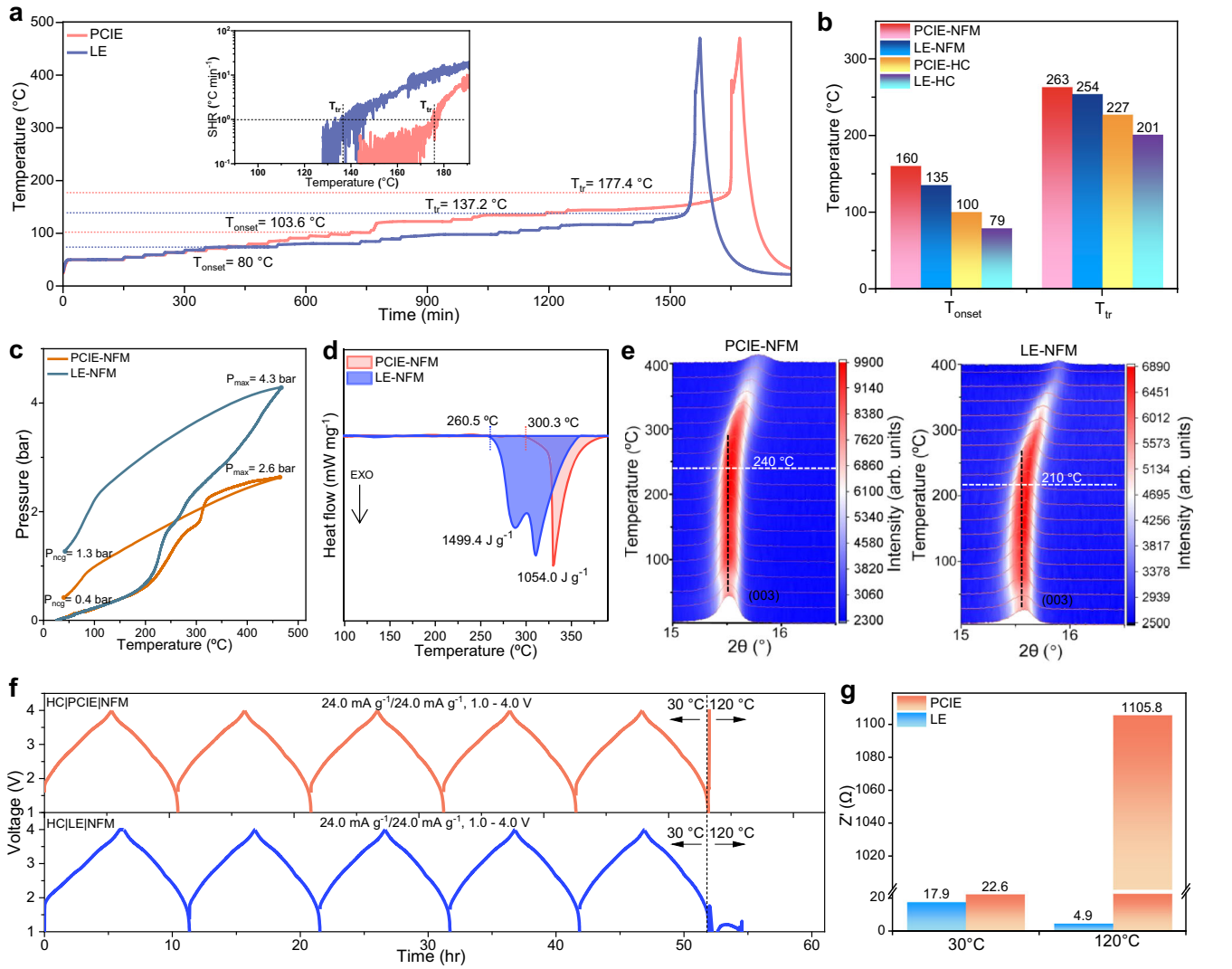

Fig. 2 | Safety enhancement of HC||NFM SIBs by smart in situ PCIE. a The time-temperature curve and self-heating rate (SHR) curve during ARC measurements of 1 Ah level pouch type HC||NFM SIBs (100% SOC) (Inset is the self-heating rate (SHR) curve. **b** T_{tr} and T_{onset} of different electrodes and electrolytes during the ARC measurements. **c** Temperature-pressure curves during the ARC test of 100% SOC NFM positive electrodes (fully desodiated NFM positive electrode). P_{ncg} and P_{max} represent the non-condensable gas pressure and the maximum pressure, respectively. **d** DSC curves of 100% SOC NFM positive electrodes. **e** In situ heating XRD for 100% SOC NFM positive electrode. **f** Voltage curves of the coin cells cycled at 24.0 mA g^{-1} for 5 cycles at 30 °C, followed by a temperature elevation to 120 °C (1.0–4.0 V) and **g** impedance variations of HC||NFM SIBs before and after heating at 120 °C for 10 min.

(Fig. 2b and Supplementary Fig. 13). In addition, the smart in situ PCIE enables the fully sodiated HC negative electrode to achieve increased T_{onset} and T_{tr} by 21 °C and 26 °C, respectively. The pressure plots obtained during the HWS test of ARC are also presented in Fig. 2c and Supplementary Fig. 14. During adiabatic heating, the LE-NFM experiences a sharp increase in gas pressure, reaching a maximum of 4.3 bar. Notably, the smart in situ PCIE-NFM effectively reduces the maximum pressure to 2.6 bar. In addition, the non-condensable gas pressure (P_{ncg}) after the cooling process is decreased from 1.3 bar to 0.4 bar by the smart in situ PCIE. During adiabatic heating, the sodiated HC negative electrode with LE experiences a sharp increase in gas pressure, and the maximum pressure is 5.1 bar. After cooling, the P_{ncg} is 2.0 bar. The P_{max} for the sodiated HC negative electrode PCIE is reduced to 3.6 bar (Supplementary Figs. 14, 15, and Supplementary Note 7). From DSC results, the smart in situ PCIE delays the heat-releasing onset temperature (from 260.5 °C to 300.3 °C) and decreases the total heat-releasing (from 1499.4 J g^{-1} to 1054.0 J g^{-1}) during the thermal runaway of the fully desodiated NFM positive electrode (Fig. 2d). As expected, the total heat released by severe exothermic reactions (located at approximately 115 °C) during the thermal runaway of the fully sodiated HC negative electrode is also reduced from 655.0 J g^{-1} to 431.3 J g^{-1} by smart in situ PCIE (Supplementary Fig. 16). Figure 2e illustrates the crystal structure evolution of the fully desodiated NFM positive electrodes through in situ heating X-ray diffraction (XRD) patterns. The XRD pattern for the fully desodiated NFM positive electrodes before heating can be indexed as P type hexagonal layered structure (space group $R\bar{3}m$). However, after the heating process, the P type layered structure undergoes a transition into a monoclinic structure[14]. The thermal-induced phase transition temperature of the fully desodiated NFM positive electrode (003) peak is postponed from 210 °C to 240 °C by smart in situ PCIE. These results also suggest that the smart in situ PCIE, with its abundance of functional groups (e.g., –CN, –NCO, and urea), can facilitate the formation of thermally stable CEI and SEI layers. In summary, the ARC and DSC results confirm that the heat release from the sodiated HC negative electrode triggers the early stage of thermal runaway, while the heat release from the desodiated NFM positive electrode accelerates the final thermal runaway of SIBs. Figure 2f shows the voltage profiles of

https://doi.org/10.1038/s41467-025-57964-7

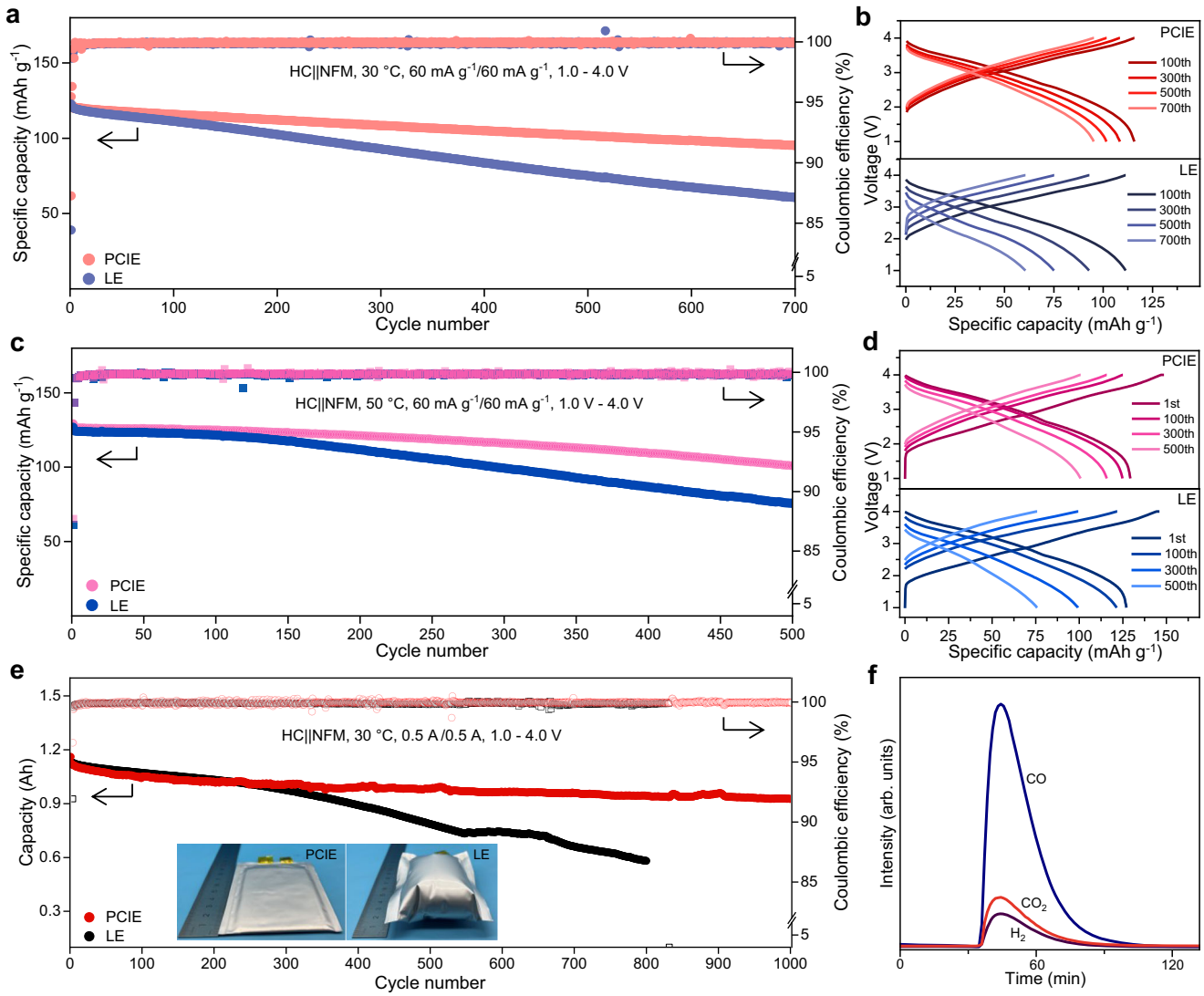

Fig. 3 | Cycle life enhancement of HC||NFM SIBs by the smart in situ PCIE. **a** Cycling performance and **b** corresponding charge-discharge curves of HC||NFM full cells (1.0–4.0 V, 30 °C). **c** Cycling performance and **d** corresponding charge-discharge curves of HC||NFM full cells (1.0–4.0 V, 50 °C). **e** Cycling performance of 1 Ah level pouch type HC||NFM cells (1.0–4.0 V, 30 °C). Insets are digital photographs of 1 Ah level pouch type HC||NFM cells cycled in the smart in situ PCIE after 1000 cycles and LE after 800 cycles, respectively. **f** Gases formed in 1 Ah level pouch type HC||NFM cells using LE for 800 cycles.

HC||NFM SIBs using smart in situ PCIE and LE cycled at 24.0 mA g^{-1} with voltage from 1.0 V to 4.0 V over 5 cycles at 30 °C. The cells are then subjected to a thermal shock test, where the temperature is raised to 120 °C. Due to the smart thermal-response cross-linking, the overall impedance of the assembled HC||NFM SIBs using the smart in situ PCIE increases from 22.6 Ω to 1105.8 Ω after heating at 120 °C for 10 min (Fig. 2g, Supplementary Fig. 17, and Supplementary Table 3). The finding indicates that the smart in situ PCIE can initiate thermal shutdown of HC||NFM cells before reaching T_{tr}, thus blocking Na^+ transportation and inhibiting the crosstalk effects of thermally induced gas species. The smart thermal-response cross-linking originates from the nucleophilic reactions of urea functional motifs in the CM main monomer with the isocyanate motif in the IM monomer. Therefore, the CM main monomer can be replaced by its methacrylate analogs containing urea, urethane, amide functional motifs, or other secondary amine-containing functional motifs. For example, a main monomer of methacrylate containing urethane and cyclic carbonate (terminal end) motifs can be also used to pair with the IM monomer to construct a smart in situ polymer electrolyte directly within SIBs (Supplementary Figs. 18–20 and Supplementary Note 8). This demonstrates the great universality of this design principle for enhancing the safety and cycle life of SIBs.

Cycle life enhancement of HC||NFM SIBs by the smart in situ PCIE

To assess potential applications, the smart in situ PCIE is directly evaluated in practical HC||NFM full cells (1.0–4.0 V) with a high NFM mass loading of 14 mg cm^{-2}. Three formation cycles at 25 mA g^{-1} were conducted for SEI formation before long-term cycling at 60 mA g^{-1} for both charge and discharge of the cells. When charged and discharged at 60 mA g^{-1} for 700 cycles at 30 °C, HC||NFM full cell using the smart in situ PCIE demonstrates a capacity retention of 79.3% (95.1 mAh g^{-1}/119.9 mAh g^{-1}) with an average coulombic efficiency of 99.93% (Fig. 3a, b). In sharp contrast, HC||NFM full cell using LE only keeps 50.5% (60.6 mAh g^{-1}/119.9 mAh g^{-1}) of its initial capacity with an average coulombic efficiency of 99.87% after 700 cycles.

When cycled at an elevated temperature of 50 °C, the smart in situ PCIE still endows the HC||NFM full cells to achieve a higher capacity retention (80.1% (100.9 mAh g^{-1}/126.0 mAh g^{-1}) compared to 61% (75.8 mAh g^{-1}/124.3 mAh g^{-1})) for the counterparts using LE over 500

https://doi.org/10.1038/s41467-025-57964-7

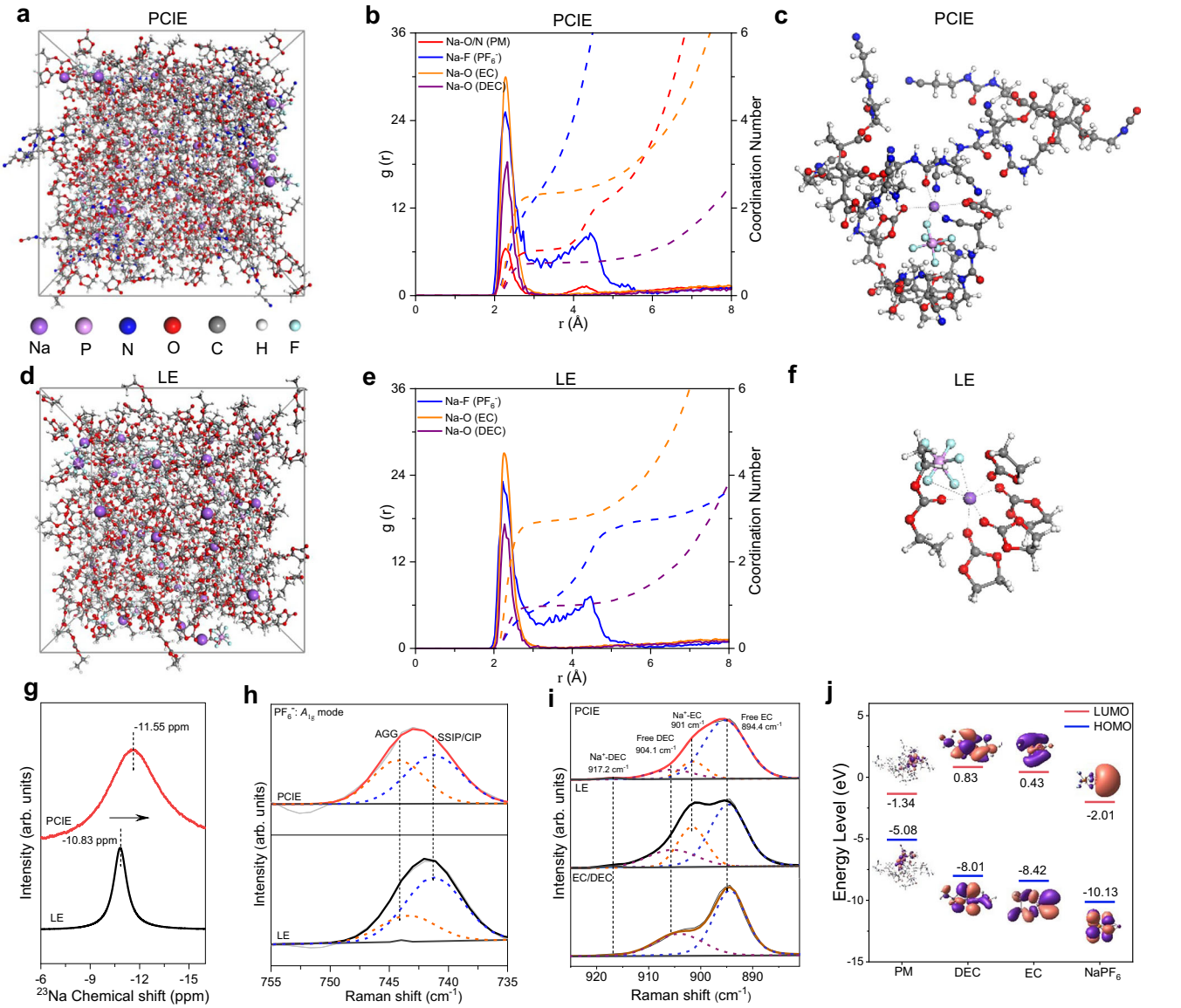

Fig. 4 | Characterizations of electrolyte solvation structures. Snapshots obtained from classical molecular dynamics simulations of **a** PCIE and **d** LE. Radial distribution functions (RDF) of **b** PCIE and **e** LE. The typical solvation structure of **c** PCIE and **f** LE. **g** ^{23}Na NMR of LE and in situ PCIE. **h** Raman spectra of PF_6^- (A1g vibration mode) of in smart in situ PCIE and LE. **i** Raman spectra of solvents and the electrolytes. **j** Calculated HOMO and LUMO energy levels of PM, EC, DEC, and $NaPF_6$.

cycles (Fig. 3c, d). More encouragingly, 1 Ah level HC||NFM pouch cells using the smart in situ PCIE demonstrate a higher capacity retention of (80%, 0.93 Ah/1.16 Ah) for 1000 cycles compared to the counterpart using LE (50.1%, 0.50 Ah/1.13 Ah) for 800 cycles at 30 °C (Fig. 3e). The as-developed smart in situ electrolyte represents an advancement among the electrolytes for HC||O3-Na_xTMO_2 SIBs, considering factors such as positive electrode mass loading, battery size and capacity, voltage range, working temperature, and safety evaluation (Supplementary Table 1). Moreover, we have implemented in situ polymerization technology directly within pouch-type HC||NFM cells. As seen from the digital images of 1 Ah HC||NFM pouch cells cycled for 1000 cycles, the smart in situ PCIE completely suppresses battery swelling, whereas the LE induces severe gas generation (insets of Fig. 3e). Mass spectrometry characterization reveals that the inhibited gas species are CO_2, CO, and H_2, originating from the decomposition of carbonate solvents (Fig. 3f). This observation suggests that the smart in situ PCIE helps form stable, robust, and passivated CEI/SEI layers, thereby blocking parasitic reactions between electrodes and electrolytes during cycling[57,58].

Electrolyte solvation structures

Uncovering the ionic solvation structure of electrolytes is favorable for figuring out the formation mechanisms of electrode/electrolyte interphases[30,47,59–61]. We performed classical molecular dynamics (MD) simulations to reveal the Na^+ solvation configurations both in PCIE and LE, which display the distributions of solvents and anions around Na^+ in the different electrolytes, as displayed in Fig. 4a–f, Supplementary Table 4, Supplementary data 1, and Supplementary Fig. 21. From the results of the snapshots (Fig. 4a, d), radial distribution function (RDF) (Fig. 4b, e and Supplementary Fig. 21), and representative solvation structures (Fig. 4c, f), we can observe that the coordination number of PF_6^- increases to 2.0, while the coordination numbers of the carbonate solvents decrease (EC to 2.2 and DEC to 0.72) in the Na^+ solvation shell of PCIE, compared to those of LE (PF_6^-, 0.96; EC, 3.0; DEC, 0.96). In

addition, the PM fragment (Supplementary Fig. 5) is also present in the Na^+ solvation shell (coordination number: 1.033), suggesting that the addition of PM fragment decreases Na^+ interactions with solvents and enhances the Na^+ interactions with PF_6^- in PCIE. On the basis, ^{23}Na NMR spectroscopy is able to distinguish the coordinating environment difference of Na^+, which corresponds to its varied solvation structure[59]. Generally, either stronger solvent binding or tighter anion binding, electronic cloud density around Na^+ will increase, leading to an up-field peak shift (more negative) in ^{23}Na NMR spectroscopy. The ^{23}Na NMR results (Fig. 4g) of in situ PCIE presents a more downfield chemical shift (−11.55 ppm) compared with that of 1 M $NaPF_6$ EC/DEC (−10.83 ppm), meaning an enhanced interaction between anions and Na^+ despite some solvents are expelled. Above MD simulation results suggest the increased contact ion pairs (Na^+ and PF_6^-), ubiquitous in high (or locally high) salt concentration electrolytes and favorable for forming protective SEI/CEI layers rich in inorganic-type species. Moreover, the results obtained from Raman spectroscopy offer additional insights into the Na^+ solvation structure of these electrolytes. On account of the different coordination states of PF_6^- anions, the Na^+ solvation structures can be generally divided into three types, solvent-separated ion pair (SSIP), Na^+–PF_6^- contact ion pair (CIP), and aggregate (AGG). From LE to PCIE, the solvation structure of AGG or CIP tends to increase along with the decreased content of SSIPs, meaning a typical feature of improved interactions between PF_6^- and Na^+ (Fig. 4h). Also, the C=O bond of PM in PCIE enters into the Na^+ solvation structure (Supplementary Note 9, Supplementary Fig. 22). As shown in Fig. 4i, the C−O bond stretching vibration peak of EC in EC/DEC mixtures is observed at 894.4 cm^{-1}. When the main conducting salt, $NaPF_6$, is added, a solvation peak related to Na^+–EC appears generates at 901 cm^{-1} [30]. This peak is weakened in the in situ PCIE, suggesting that fewer solvents coordinate with Na^+ in this environment, consistent with the MD simulation results. Calculations of the frontier molecular orbital energy are then performed to evaluate the reduction and oxidation stability of each electrolyte component (Supplementary data 2). The lowest unoccupied molecular orbital (LUMO) energy of $NaPF_6$ (−2.01 eV) and PM fragment (−1.34 eV) is lower than that of EC (0.43 eV) and DEC (0.83 eV) (Fig. 4j). Consequently, foreign electrons are more likely to occupy their lower energy orbitals, enabling easier reduction and involvement of $NaPF_6$ and PM fragment in forming SEI layers[61]. The enhanced coordination between Na^+ and PF_6^- in the solvation structures of in situ PCIE is beneficial to anionic decompositions and thus to form protective NaF, which passivates the HC negative electrode. Moreover, the highest occupied molecular orbital (HOMO) energy level of the PM fragment (−5.08 eV) is higher than that of EC (−8.42 eV), DEC (−8.01 eV), and $NaPF_6$ (−10.13 eV). This indicates that the PM fragment is more susceptible to oxidation, which leads to the formation of a beneficial CEI layer on the NFM positive electrode (Fig. 4j). In summary, in situ PCIE exhibits a unique solvation structure, where the Na^+ solvation shell is enriched with PF_6^- anions and the PM fragment, demonstrating the ability to form protective SEI/CEI layers. This will be discussed in the following parts.

Characterizations of NFM positive electrode cycled in the smart in situ PCIE

To understand the mechanisms underlying the cycling stability and enhanced thermal safety of SIBs using smart in situ PCIE, the NFM positive electrode and HC negative electrodes are disassembled from discharged HC||NFM full cells that have been cycled at 50 °C for 200 cycles. The field-emission scanning electron microscopy (SEM) images indicate that NFM particles maintain their integrity without cracking when cycled in the as-fabricated smart in situ PCIE (Fig. 5a). In contrast, the NFM particles exhibit severe microcracking when cycled in LE (Fig. 5b). The formation of unique microcracking is closely associated with active sodium loss, irreversible phase transitions, and TM dissolution[62]. As observed from high-resolution transmission electron microscopy (HRTEM) images (Fig. 5c, d), smart in situ PCIE favors the formation of a thinner and more homogeneous CEI layer on NFM positive electrode, indicating the alleviated electrolyte oxidative decompositions. The HRTEM images also indicate that the surface layered crystal structure of the NFM positive electrode is better preserved when cycled in the smart in situ PCIE. Active sodium loss will result in inefficient intercalation of Na^+ back into the layered structure, leading to enhanced electrostatic interactions (O–O) within the layered structure of the NFM positive electrode, accompanied by a lower angle shift of the (003) peak[14]. Obviously, the (003) peak of the NFM positive electrode cycled in LE shifts to lower angles than the counterpart using smart in situ PCIE (Fig. 5e).

To evaluate TMs dissolution behaviors, fully charged NFM positive electrodes are immersed in LE and stored at 50 °C for 12 h. Inductively coupled plasma optical emission spectrometry (ICP-OES) results suggest that TMs dissolutions are alleviated when the NFM positive electrode is fully charged in smart in situ PCIE (Supplementary Fig. 23 and Supplementary Note 10), indicating the formation of a thermally robust CEI layer. The suppressed TMs dissolution is also revealed by synchrotron X-ray tomography of HC||NFM full cells (Supplementary Fig. 24 and Supplementary Note 11). The electronic structures of Mn ions in the NFM positive electrodes are investigated by measuring the soft X-ray adsorption spectroscopy (SXAS) at $L_{2,3}$-edges of 3d elements in the total electron yield (TEY) mode (with a probing depth of about 5 nm). The energy position and multiplet spectral feature of the 3d TM $L_{2,3}$ SXAS spectra are highly sensitive to their valence state[63,64] and local environment[65–67]. Figure 5f–h shows the Mn $L_{2,3}$-edge SXAS spectra of the pristine NFM, NFM positive electrode cycled in smart in situ PCIE and LE, and those of MnS, $LaMnO_3$, and Li_2MnO_3 as Mn^{2+}, Mn^{3+}, and Mn^{4+} references, respectively. In Fig. 5f, the Mn $L_{2,3}$ SXAS spectrum of the pristine NFM sample is nearly the same as that of Li_2MnO_3[68], suggesting that the Mn ions valence state is close to Mn^{4+} in the pristine NFM. The Mn-$L_{2,3}$ SXAS spectrum of the NFM positive electrode cycled in smart in situ PCIE becomes poorly resolved due to the mixed valence state of Mn ion (Fig. 5g). In the case of mixed valence Mn oxide, the average valence state can be obtained by simple supposition of spectra from different valence states[69,70]. The quantitative Mn valence state can be obtained by superpostion of references. Figure 5g shows the ratio of Mn^{4+} to Mn^{3+} is 0.78:0.22, demonstrating an average valence state of $Mn^{3.78+}$ on the surface of the NFM positive electrode cycled in smart in situ PCIE. In Fig. 5h, the Mn $L_{2,3}$ SXAS spectrum of the NFM cycled in LE is nearly the same as that of MnS[71,72], suggesting the Mn ions valence state is close to Mn^{2+}. It is worth mentioning that low-valence transition metals can be easily dissolved into electrolytes[41,53]. Therefore, when using smart in situ PCIE, a thin and homogeneous CEI layer inhibits the reduction of the TMs' oxidation state, ultimately preventing their dissolution from the NFM positive electrode. In-depth N 1*s* X-ray photoelectron spectroscopy (XPS) analysis demonstrates that the CEI layer of NFM positive electrodes cycled in PCIE is enriched with cyano (398.8 eV), -NCO (400.4 eV), and urea (399.8 eV) functional groups, which can generate stable complexations to prevent the TMs dissolution and suppress electrolyte oxidative decomposition (Fig. 5i)[53,73–75]. With increasing etching depth in PCIE, the peak intensity of nitrogen-containing components increases, which aligns with the results from detailed C 1*s* XPS analysis. This finding is consistent with the HOMO energy level calculations, indicating that the PM fragment is prone to decomposition on the positive electrode side. Oxygen-containing compounds, such as C–O/C=O, are identified in the O 1*s* spectra (Fig. 5j). The C 1*s* XPS spectra of NFM positive electrodes reveal a higher peak intensity of C–C bonds in LE (Fig. 5k), suggesting significant side reactions involving organic solvents in LE. Compared to LE, NFM positive electrodes in PCIE exhibit reduced peak intensity C–C bonds in C 1*s*, suggesting less electrolyte decomposition and a thinner SEI layer when using PCIE. As envisioned by F 1*s* XPS spectra

https://doi.org/10.1038/s41467-025-57964-7

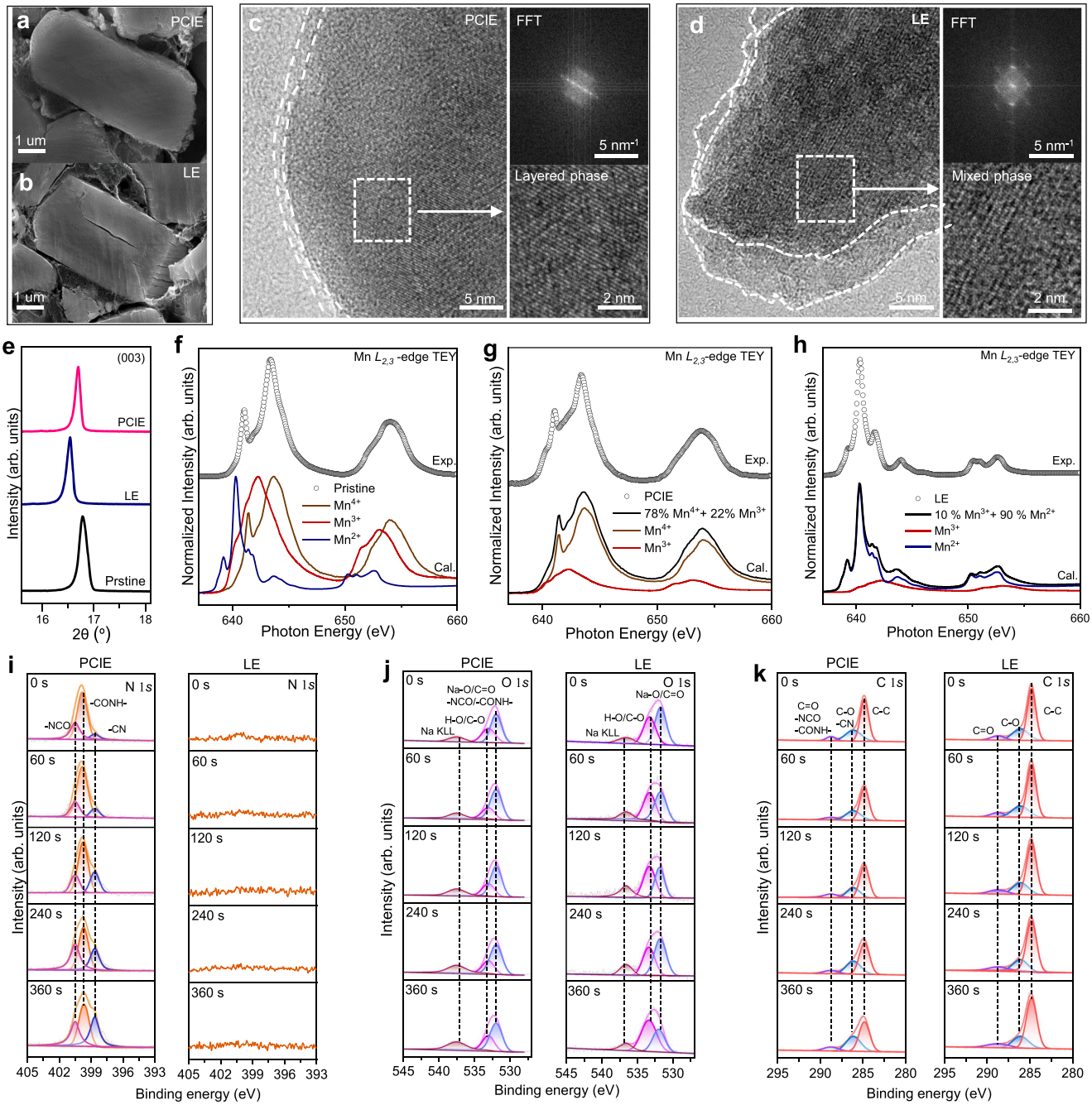

Fig. 5 | Characterizations of NFM positive electrode cycled in the smart in situ PCIE at the elevated temperature. Typical SEM images of NFM positive electrodes cycled in **a** the smart in situ PCIE and **b** LE. HRTEM images of NFM positive electrodes cycled in **c** the smart in situ PCIE and **d** LE. **e** XRD patterns of cycled NFM positive electrodes. Mn $L_{2,3}$-edge XAS spectra in TEY mode for **f** the pristine NFM positive electrode and MnS, $LaMnO_3$, and Li_2MnO_3 as Mn^{2+}, Mn^{3+}, and Mn^{4+} references, respectively, and the NFM positive electrode at discharged state cycled in **g** the smart in situ PCIE and **h** LE. **i** In-depth XPS spectra of N 1*s*, **j** O 1*s*, and **k** C 1*s* XPS spectra of cycled NFM positive electrodes. The NFM positive electrodes are disassembled from the HC||NFM full cells, which are cycled at 60 mA g^{-1} for 200 cycles at 50 °C in the discharged state.

(Supplementary Fig. 25), the decomposition of carbonate solvents and $NaPF_6$ salt on NFM positive electrodes is greatly inhibited when using smart in situ PCIE. Furthermore, there are no significant changes in the content of decomposition products on the cycled PCIE-based NFM positive electrodes with increasing etching depth. These results show that PM suppress solvent/salt decomposition, forming a more uniform and relatively thinner CEI, as evidenced by TEM images of the CEI layer on the NFM positive electrode (Fig. 5c, d). In contrast, the CEI when using LE exhibits nonuniform, thick morphologies, which may be attributed to increased oxidation decomposition of salts and solvents.

Characterizations of HC negative electrode cycled in smart in situ PCIE

Apart from the CEI layer, the SEI layer on the HC negative electrode also affects the safety and cycle life of SIBs[15]. Then, the effects of the smart in situ PCIE on the SEI layer of the HC negative electrode are comprehensively investigated. From the HRTEM images (Supplementary Fig. 26), smart in situ PCIE favors the formation of a thinner and more homogeneous SEI layer on the HC negative electrode, suggesting the alleviated reductive decomposition of electrolytes. To gain more insights into the SEI compositions, the depth profiles of XPS are

https://doi.org/10.1038/s41467-025-57964-7

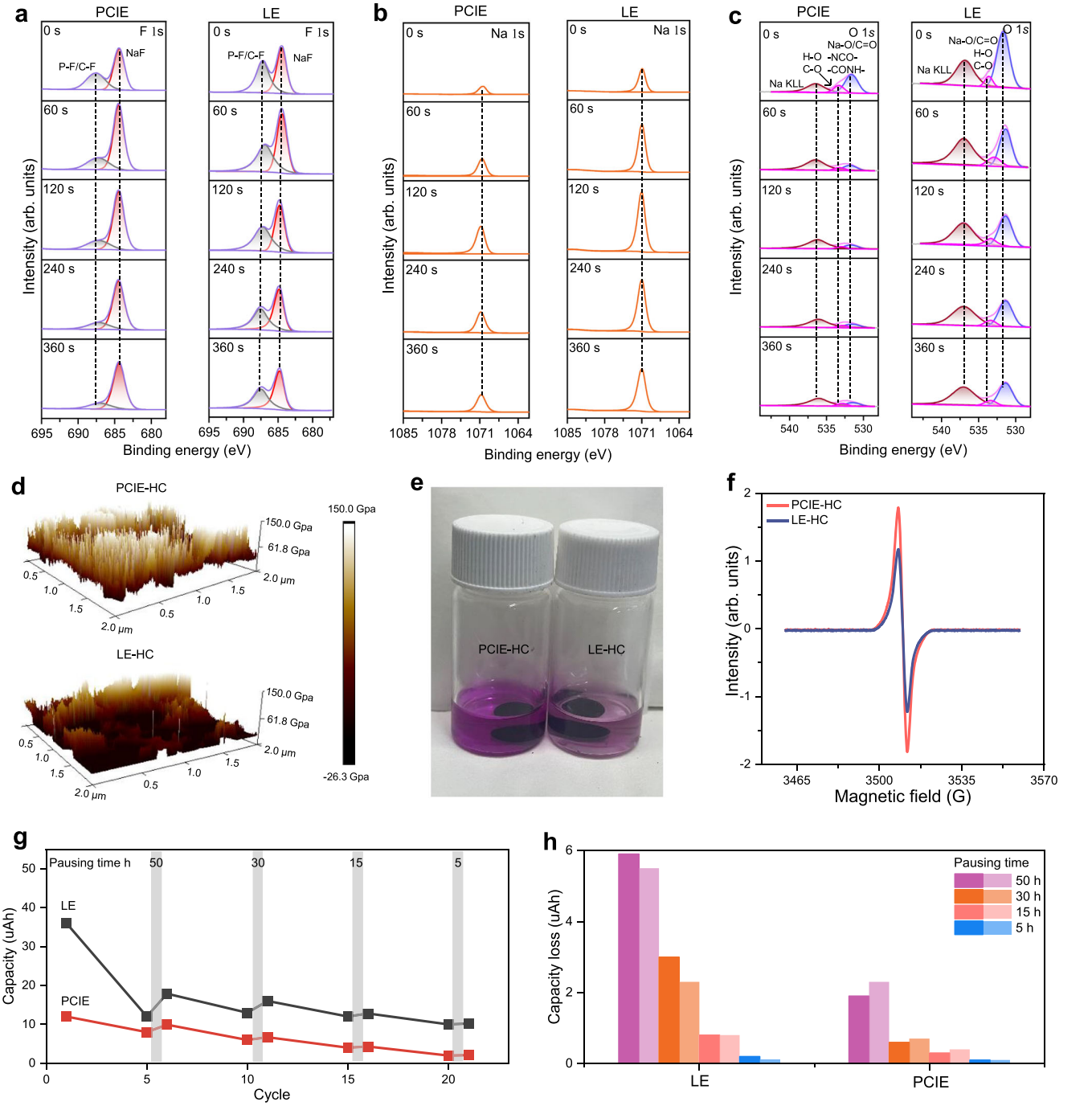

Fig. 6 | Characterizations of HC negative electrode cycled in the smart in situ PCIE. In-depth XPS spectra of **a** F 1*s*, **b** Na 1*s*, and **c** O 1*s* of cycled HC negative electrodes which are cycled at 60 mA g^{-1} for 200 cycles at 50 °C in discharged state. **d** Surface Young's modulus mappings of the HC negative electrode which are cycled at 60 mA g^{-1} for 200 cycles at 50 °C in discharged state. **e** The optical photograph of fully sodiated HC negative electrode cycled at 60 mA g^{-1} for 200 cycles soaked in the ethanol solution containing 1% phenolphthalein. **f** EPR spectra of fully sodiated HC negative electrodes which are cycled at 60 mA g^{-1} for 200 cycles at 50 °C. **g** The average capacity variations of Na||Cu cells from the electrolyte reductive reactions before and after each pause time as a function of cycle numbers. The gray area with width represents cell pause processes. The average capacity is the average of the two parallel cells. **h** Capacity loss of Na||Cu cells with different pause times in smart in situ PCIE and LE.

obtained by carrying out Ar^+ sputtering for 0 s, 60 s, 120 s, 240 s, and 360 s. In Fig. 6a, the enrichment of inorganic NaF suggests that the SEI layer dissolution issues can be greatly alleviated by smart in situ PCIE[15,76]. Moreover, the decreased formation of P-F species (687.6 eV, F 1*s*) indicates that the overall decomposition of $NaPF_6$ in electrolytes is greatly reduced despite the preferential decomposition of $NaPF_6$. The decreased Na-containing species in the SEI layer suggests that the active sodium loss at the HC negative electrode is greatly alleviated by the smart in situ PCIE (Fig. 6b). The O 1*s* XPS analysis of the HC electrode reveals the presence of oxygen-containing compounds, such as C–O/C=O (Fig. 6c). Peaks at 533.1 eV (assigned to C–O/H–O) and 531.8 eV (assigned to C=O/Na–O) correspond to organic species $ROCO_2Na$ and $(CH_2OCO_2Na)_2$, which are likely products of reductions reactions involving Na^+-solvent complexes[47]. Compared to LE, the HC electrode in PCIE exhibits a reduced O 1*s* peak intensity compared to that in LE, suggesting less electrolyte decomposition and a thinner SEI

layer (Fig. 6c). The smart in situ PCIE promotes the formation of a more uniform SEI layer on the HC negative electrode, as evidenced by C 1*s* XPS (Supplementary Fig. 27). The contents in C 1*s* within the SEI layer of the smart in situ PCIE remains consistent across varying depths, indicating a more uniform SEI layer formed on the HC electrode. In contrast, the contents of C 1*s* within the SEI layer of the LE exhibit substantial fluctuations with etching duration. The participation of N-containing species in modifying the negative electrode SEI layer is revealed by the presence of cyano, -NCO, and urea signals in Supplementary Fig. 28. Based on the XPS results, the enhanced electrochemical and thermal stability of the HC negative electrode can be attributed to the formation of a robust SEI layer enriched with N-containing species and high modulus NaF species.

In addition, this explains why the Young's modulus of the HC negative electrode cycled in the smart in situ PCIE (36.3 GPa) is higher than that of the negative electrode cycled in LE (19.5 GPa), as measured by atomic force microscopy (AFM) (Fig. 6d). This enrichment helps to withstand the plastic deformation of HC negative electrode, alleviate parasitic reactions, and maintain the electrode integrity upon cycling. Apart from this, smart in situ PCIE forms robust SEI layer of HC negative electrodes, preventing the side reaction between the electrolyte and the sodium clusters in the HC negative electrode, accelerating the formation of quasi-metallic Na clusters at the low potential region (Fig. 6e, f). To be specific, taking advantage of the specific reaction of the fully sodiated HC negative electrode with a protic solvent (ethanol), the quasi-metallic feature of the steady-state sodium in HC can be revealed by the alkalinity semiquantitatively indicated by 1% phenolphthalein solution. The solution obtained from the reaction between ethanol and the HC negative electrode fully sodiated using smart in situ PCIE is more alkaline (Fig. 6e), suggesting the formation of more quasi-metallic Na clusters in HC negative electrode under the help of smart in situ PCIE. Electron paramagnetic resonance (EPR) is applied for the detection of unpaired electrons of fully sodiated HC negative electrode. Fully sodiated HC negative electrode in smart in situ PCIE electrolyte delivers a sharper intensity peak (Fig. 6f), also indicative of the facilitated formation of quasi-metallic Na clusters in HC negative electrode. In short, the SEI layer formed in smart in situ PCIE is thin and mechanically robust, resulting in decreased electrolyte reductive decompositions of the HC negative electrode.

To assess the effect of smart in situ PCIE in suppressing the SEI layer dissolution, the capacity loss of Na||Cu cells using smart in situ PCIE and LE are determined for direct comparison[22]. In the test, the Na||Cu cells are cycled in the voltage range of 0.005–2 V to form the SEI layer on the Cu surface (Fig. 6g, Supplementary Fig. 29, and Supplementary Note 12). Then, the Na||Cu cells are paused at the 2 V for x h (x = 50 h, 30 h, 15 h, and 5 h) after every five cycles to illustrate SEI layer dissolution, and then continued for later cycling. The capacity increase of Na||Cu cells after every pause mainly results from the reductive electrolyte decomposition to compensate the SEI layer dissolution during the prolonged open-circuit pauses (Fig. 6g). The capacity reduction (i.e., the difference between the capacity after and before each pause can quantify SEI dissolution. The smart in situ PCIE renders the lower capacity reduction at every pause (Fig. 6h), which enables greatly alleviated SEI dissolution contributing to the enhanced safety and extended cycle life of SIBs.

In summary, a smart in situ PCIE has been constructed in sustainable HC||O3-NFM SIBs through thermally-induced in situ radical polymerization of CM and IM monomers dissolved in LE. Smart in situ PCIE with functional motifs of cyano, isocyano, and urea can facilitate the formation of robust electrode/electrolyte interphase layers, alleviating electrolyte decompositions and increasing the thermal stability of electrodes. Inspiringly, ARC shows that in situ PCIE endows HC||NFM pouch cells with an increased T_{onset} and T_{tr} by 23.6 °C and 40.2 °C, respectively. The smart in situ PCIE is characterized by further covalent cross-linking via the addition reactions between urea and isocyanate when the temperature exceeds 120 °C, which helps to block the ion transportation and inhibits crosstalk effects, thus enhancing the safety of sustainable SIBs. In addition, the smart in situ PCIE enhances the longevity of HC||NFM full cells, particularly under elevated temperature conditions. This design approach for creating in situ formed smart gel polymer electrolytes represents a milestone in the pursuit of high-safety, long-life sustainable SIBs.

Methods

Materials

Isocyanate-based methacrylate (IM, 98%), triethylamine (99%) and aminopropionitrile (AN, 98%) were purchased from Meryer Chemical Technology Co., Ltd. N-Methyl-2-pyrrolidone (NMP, >99.0%), chloroform-d (CCl_3D, 100% 99.96 atom% D, 0.03% (v/v) TMS), dichloromethane (≥99.5%) and azobisisobutyronitrile (AIBN, ≥99%) were obtained from Aladdin without further purification. Polyvinylidene difluoride (PVDF) was purchased from Solvay S.A. Co. Super P (TIMCAL) was used after being dried in an oven at 120 °C for 12 h. The conventional liquid electrolyte of 1.0 M $NaPF_6$ in ethylene carbonate (EC)/diethyl carbonate (DEC) (1:1 by volume) was obtained from Suzhou DoDo Chem Technology Co., Ltd. $NaNi_{1/3}Fe_{1/3}Mn_{1/3}O_2$ (NFM) was provided by Jiangsu Xiangying New Energy Technology Co., Ltd. Hard carbon (HC) was purchased from the Kuraray Co. Ltd., Japan. Carboxymethylcellulose sodium (CMC, DAICEL Investment Co., Ltd.) and styrene butadiene rubber (SBR, Nippon & L Inc.) were used as purchased. The PC3D012028-type separator with a porosity of 43%, was procured from DINHO TECHNOLOGY Co., Ltd. The aluminum foil current collector with a thickness of 12 μm was purchased from NANSHAN LIGHT ALLOY Co., Ltd. without any further treatment.

Synthesis of CM monomer

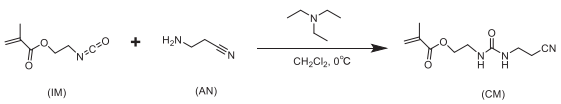

(1)

The synthesis of CM is presented via the Eq. 1. To a 250 mL three-neck flask equipped with a magnetic stir bar in the atmosphere of nitrogen, 0.3 mL of triethylamine, 3.5 g of AN (liquid) and 120 mL of dichloromethane were added and then cooled by an ice-water bath. Subsequently, 7.75 g of IM (liquid) was added dropwise to the mixture, which was then stirred continuously overnight. After quenching the reaction with deionized water, the organic phase was sequentially washed with 1 wt% aqueous sodium hydroxide solution, 1 wt% aqueous hydrochloric acid solution, and saturated aqueous sodium chloride solution, followed by drying over anhydrous magnesium sulfate. The resultant mixture was then filtered, and the solvent was removed via rotary evaporation. The crude product was subsequently purified by recrystallization from a dichloromethane/n-hexane mixture (1:2 by volume). The final white solid product, designated as CM, was isolated with a mass of 10.0 g, corresponding to a yield of 88.9%. Corresponding ^{1}H NMR and ^{13}C NMR can be seen from Supplementary Figs. 1 and 2. For CM, ^{1}H NMR (600 MHz, ^{d}DMSO): δ 6.32 (t, *J* = 6.0 Hz, 1H), 6.21 (t, *J* = 6.0 Hz, 1H), 6.06 (dt, *J* = 1.8, 1.2 Hz, 1H), 5.68 (t, *J* = 1.8 Hz, 1H), 4.06 (t, *J* = 6.0 Hz, 2H), 3.29 (q, *J* = 6.0 Hz, 2H), 3.23 (q, *J* = 6.0 Hz, 2H), 2.59 (t, *J* = 6.0 Hz, 2H), 1.88 (t, *J* = 1.2 Hz, 3H). ^{13}C NMR (151 MHz, ^{d}DMSO): δ 166.97, 158.21, 136.34, 126.18, 119.98, 64.43, 38.72, 36.20, 18.99, 18.37. HRMS (m/z): $[Na]^+$ calcd. for $C_{10}H_{15}N_3O_3$, 248.1011; found, 248.1016.

Preparation of gel polymer electrolyte

The gel polymer electrolyte (PCIE) was synthesized through in situ thermally initiated radical polymerization. The precursor solution was prepared by mixing CM, IM, and 1 M $NaPF_6$ in EC/DEC at a mass ratio of

4:1:25 at room temperature for 0.5 h. Subsequently, 1 wt% AIBN was added to the homogeneous solution and stirred for an additional 15 min. The electrolyte precursor was then injected into coin-type and pouch-type full cells, which were subsequently heated at 60 °C for 8 h.

Prepare electrodes and assemble battery

The high-mass-loading dry positive electrode comprised 94.5 wt% NFM, 3 wt% Super P, and 2.5 wt% PVDF binder. The positive electrode slurry was coated onto an aluminum foil current collector and subsequently dried under vacuum conditions at 110 °C for 24 h. The average mass loading of active NFM positive electrode was 14 ± 0.2 mg cm^{-2}. The corresponding high-mass-loading dry negative electrode comprised 94.8 wt% HC, 2 wt% Super P, 1.2 wt% CMC, and 2 wt% SBR. The negative electrode slurry was coated by automatic coating machine onto an aluminum foil current collector and subsequently dried under vacuum conditions at 100 °C for 24 h. The N/P ratio of HC (2.07 mAh cm^{-2}, 300 mAh g^{-1})||NFM (1.71 mAh cm^{-2}, 120 mAh g^{-1}) full cell was about 1.2. For coin-type cells, the electrodes were punched into disks with diameters of 12 mm for the positive electrode and 14 mm for the negative electrode, respectively. The HC||NFM 2032 coin-type full cells were assembled using the as-prepared NFM positive electrodes and HC negative electrodes, with 100 µL of electrolyte, in an argon-filled glovebox where the oxygen and water contents were maintained below 0.01 ppm. The assembly of the 7-layer HC||NFM pouch-type cells was conducted within a glove box, with nickel and aluminum tabs securely fastened to the negative electrode and positive electrodes, respectively. Use an automatic cutting machine to cut the electrodes to the correct dimensions. The dimensions of the positive electrodes were recorded as 58 mm × 82 mm, while the negative dimensions were measured at 60 mm × 84 mm. Subsequent to this, the electrodes and the separator were laminated together and assembled into aluminum plastic film bags, which were then sealed under vacuum. Electrolyte precursor (8 mL) was then injected into one pouch-type full cell, which were subsequently heated at 60 °C for 8 h. The pouch-type full cells were then degassed after ageing for 12 h at 60 °C and the first cycles. Pouch-type cells were tested under 1 MPa pressed by splint.

Electrochemical measurements

The Na^+ transference number (t_{Na^+}) was obtained by a chronoamperometry test with a voltage amplitude of 0.01 V using Na||Na cells at 30 °C, and EIS tests were performed before and after DC polarization at 30 °C. The value of t_{Na^+} was calculated by using the following equation:

$$t_{Na^+} = \frac{I_{ss}}{I_0} \cdot \frac{(V - I_0 R_0)}{(V - I_{ss} R_{ss})} \quad (2)$$

where I_0 and I_S are the initial and steady-state DC currents, respectively, R_0 and R_S are the interfacial resistances of the initial and steady states, and ΔV is the applied potential. Electrochemical impedance spectroscopy (EIS) was conducted within the frequency range of 7 MHz to 100 mHz utilizing an AC amplitude of 10 mV with 6 points per decade at 30 °C (potentiostat with frequency response analyzer, Biologic VMP-300). AC impedance measurements were performed after open-circuit potential for 10 min. The ionic conductivity values of the electrolytes were calculated using the equation σ = L/RS, where L represents the thickness of the separator, S denotes the area of the separator, and R is the bulk electrolyte resistance obtained from the electrochemical impedance spectroscopy (EIS) of symmetrical stainless-steel/stainless-steel cells (with an AC amplitude of 10 mV, over a temperature range of 30 to 90 °C). The electrochemical stability window of the electrolytes was estimated by a linear sweep voltammetry (LSV) test at a scan rate of 10 mV s^{-1} from 0.0 V to 6.0 V at 30 °C. The cycling performance of the batteries was evaluated using a LAND testing system (Wuhan LAND Electronics Co., Ltd.) at 30 °C and 50 °C, respectively. The C-rates for the electrochemical measurements, within the voltage range of 1.0 to 4.0 V, were defined based on a value of 1 C equating to 120 mA g^{-1}.

Characterizations

Fourier transform infrared spectroscopy (FTIR) and nuclear magnetic resonance (NMR) spectra of the samples were acquired using the Bruker VERTEX 70 and Bruker AVANCE III 400 MHz instruments, respectively. Molecular weights of polymer were measured through gel permeation chromatography (GPC, an Agilent 1260 Infinity Lab II GPC fitted with a refractive index detector at 35 °C using a single Agilent polar gel column equipped with an oven at 35 °C). In the testing process, polymer samples were dissolved in the DMSO eluent (2.0 mg mL^{-1}) and then filtered (0.2 µm pore size) and eluted immediately at a flow rate of 1.0 mL min^{-1}. Field-emission scanning electron microscopy (SEM, Hitachi S-4800 at 10 kV) and high-resolution transmission electron microscopy (HRTEM, Tecnia G20, FEI) were utilized to examine the morphologies of the samples. X-ray diffraction (XRD) was carried out by Ultima IV diffractometer (Rigaku) with Cu Kα radiation (λ = 1.5406 Å). Argon plasma etching X-ray photoelectron spectroscopy (Ar-XPS, Thermo Scientific ESCA Lab 250Xi) was employed to characterize the positive electrode electrolyte interphase (CEI) and solid electrolyte interphase (SEI) layers. All the XPS samples were transferred by the vacuum device. Inductively coupled plasma optical emission spectrometry (ICP-OES, Optima 8300) was employed to evaluate the dissolution of transition metals (Ni, Fe, and Mn) from the fully charged positive electrodes when soaked in the electrolyte for 12 h at 50 °C. These positive electrodes were disassembled from the HC||NFM cells, which had been cycled using various electrolytes for 200 cycles at a 0.5 C rate. Accelerating rate calorimeter (ARC, BTC-130) technology was employed to examine the thermal behaviors of electrolytes and the thermal runaway characteristics of HC||NFM pouch cells with varied electrolytes. For the signals of varied gases during the ARC test process, the released gases are monitored by mass spectrometry (MS, HPR-20). For the ortho-positronium (o-Ps) annihilation was analyzed using positron annihilation lifetime spectroscopy (PALS, ORTEC, ^{22}Na). The investigation was carried out under a heating increment of 5 °C and a waiting period of 20 min. The thermal stability of the electrodes was analyzed using differential scanning calorimetry (DSC, NETZSCH DSC 214, Polvma).

The gas produced in the pouch cells was collected using an airbag and subsequently analyzed for its composition utilizing mass spectrometry (MS, HPR-40, Hiden Analytical). The topography and modulus images of the cycled electrodes were obtained using an atomic force microscopy (AFM) system (Bruker Corp., Dimension Icon). Electron paramagnetic resonance (EPR) spectra were collected using a Bruker Emx PLUS spectrometer (active material loading of each HC negative electrode in the analysis of EPR for sodium clusters is 7.3 mg/cm^2). Soft X-ray absorption spectroscopy (SXAS) of pristine and cycled NFM positive electrodes at the Mn $L_{2,3}$-edge in total electron yield (TEY) mode was performed at Beamline (BL) 11 A of the National Synchrotron Radiation Research Center (NSRRC) in Taiwan.

Synchrotron X-ray Tomography Measurement: The tomography cells (tomo-cells) after 100 cycles in the discharged state were analyzed at the P05 beamline at DESY, Hamburg, Germany, using synchrotron radiation monochromatized with a double multilayer monochromator (DMM). The X-rays were converted to visible light using a 100-µm-thick $CdWO_4$ single crystal scintillator. A fast KIT CMOS camera (5120 × 3840 pixels) was employed and kept out of the direct beam using a mirror. The measurement included 2400 projections within a 180° battery rotation, with an exposure time of 25 ms per projection. The field of view (FOV) was 3.28 × 2.46 mm^2, with a pixel size of 0.65 µm. It is important to note that a binning process of 2 by 2 was employed during the reconstruction of the dataset to achieve a

high signal-to-noise ratio, resulting in a spatial resolution of 1.3 μm. The raw tomography data given by DESY was then handled by employing in-house reconstruction software programmed in IDL 8.2. These data need to be normalized and de-noised, and to be filtered in some cases before using for the final reconstruction. The reconstruction data were processed using the ImageJ. Avizo was used to generate the 3D renderings shown in the current work.

Density functional theory calculation

All calculations were conducted using the Gaussian 16 program. Density functional theory (DFT) geometry optimizations utilized the B3LYP-D3 functional in conjunction with def2-SVP basis sets. Frequency calculations were conducted at the same theoretical level as the geometry optimizations to confirm that the stationary points are indeed minima. In order to obtain more accurate energy values, single-point energies were calculated using the B3LYP-D3 functional with the def2-TZVP basis set. These calculations were performed to determine the HOMO-LUMO gap energy.

Molecular dynamic simulations for solvation structure analysis

Molecular dynamics (MD) simulations were conducted to investigate the solvation structures of the two considered electrolyte systems, namely LE and PCIE. The two electrolyte systems, each comprising different numbers of components (as detailed in Supplementary Table 4), were constructed into cubic simulation boxes. All MD simulations were performed using the Forcite module with the COMPASS III force field[77,78]. Van der Waals and Coulomb interactions were respectively considered by atom based and Ewald methods with a cut-off value of 12.5 Å. Equations of motion were integrated with a time step of 1 fs. After energy minimization, each system was fully relaxed under periodic boundary conditions for 400 ps in the NPT (P = 1 atmosphere, T = 303 K) ensemble using the Nose thermostat and Berendsen barostat, which was long enough for system temperature, potential, and total energy to get stable. After reaching the equilibrium state, another 5000 ps simulation under NVT ensemble was performed to extract trajectory and data for radial distribution function (RDF) and coordination number (CN) calculation. The dynamic trajectory for each system was outputted at an interval of 5 ps. The coordination number N_i of molecules i in the first solvation shell surrounding Na^+ was calculated as:

$$N_i = 4\pi\rho \int_0^{R_M} g(r) r^2 dr \tag{3}$$

in which R_M is the distance of the first minimum following the first peak in the RDF $g(r)$ and ρ is the number density of molecules i[79].

Data availability

The XX data generated in this study are provided in the Supplementary Information/Source data file. Source data are provided with this paper.

References

1. Wang, J. et al. Fire-extinguishing organic electrolytes for safe batteries. *Nat. Energy* **3**, 22–29 (2017).
2. Sun, H. et al. A safe and non-flammable sodium metal battery based on an ionic liquid electrolyte. *Nat. Commun.* **10**, 3302 (2019).
3. Bray, J. M. et al. Operando visualisation of battery chemistry in a sodium-ion battery by ^{23}Na magnetic resonance imaging. *Nat. Commun.* **11**, 2083 (2020).
4. Su, Y. et al. Rational design of a topological polymeric solid electrolyte for high-performance all-solid-state alkali metal batteries. *Nat. Commun.* **13**, 4181 (2022).
5. Li, Y. et al. Interfacial engineering to achieve an energy density of over 200 Wh kg^{-1} in sodium batteries. *Nat. Energy* **7**, 511–519 (2022).
6. Tang, Z. et al. Revealing the closed pore formation of waste wood-derived hard carbon for advanced sodium-ion battery. *Nat. Commun.* **14**, 6024 (2023).
7. He, J. et al. Tuning the solvation structure with salts for stable sodium-metal batteries. *Nat. Energy* **9**, 446–456 (2024).
8. Rudola, A. et al. Opportunities for moderate-range electric vehicles using sustainable sodium-ion batteries. *Nat. Energy* **8**, 215–218 (2023).
9. Usiskin, R. et al. Fundamentals, status and promise of sodium-based batteries. *Nat. Rev. Mater.* **6**, 1020–1035 (2021).
10. Liang, X. et al. Practical cathodes for sodium-ion batteries: who will take the crown? *Adv. Energy Mater.* **13**, 2301975 (2023).
11. Li, Y. et al. Origin of fast charging in hard carbon anodes. *Nat. Energy* **9**, 134–142 (2024).
12. Wang, X. et al. Achieving a high-performance sodium-ion pouch cell by regulating intergrowth structures in a layered oxide cathode with anionic redox. *Nat. Energy* **9**, 184–196 (2024).
13. Zhao, C. et al. Rational design of layered oxide materials for sodium-ion batteries. *Science* **370**, 708–711 (2020).
14. Xie, Y. et al. Probing thermal and chemical stability of $Na_xNi_{1/3}Fe_{1/3}Mn_{1/3}O_2$ cathode material toward safe sodium-ion batteries. *Chem. Mater.* **30**, 4909–4918 (2018).
15. Liao, Y. et al. Pentafluoro(phenoxy)cyclotriphosphazene stabilizes electrode/electrolyte interfaces for sodium-ion pouch cells of 145 Wh kg^{-1}. *Adv. Mater.* **36**, 2312287 (2024).
16. Che, H. et al. Engineering optimization approach of nonaqueous electrolyte for sodium ion battery with long cycle life and safety. *Green. Energy Environ.* **6**, 212–219 (2021).
17. Zhou, Q. et al. Thermal stability of high power 26650-type cylindrical Na-ion batteries. *Chin. Phys. Lett.* **38**, 076501 (2021).
18. Yang, C. et al. Materials design for high-safety sodium-ion battery. *Adv. Energy Mater.* **11**, 2000974 (2021).
19. Ding, F. et al. Using high-entropy configuration strategy to design Na-ion layered oxide cathodes with superior electrochemical performance and thermal stability. *J. Am. Chem. Soc.* **144**, 8286–8295 (2022).
20. Mogensen, R. et al. Solubility of the solid electrolyte interphase (SEI) in sodium ion batteries. *ACS Energy Lett.* **1**, 1173–1178 (2016).
21. Ma, L. A. et al. Strategies for mitigating dissolution of solid electrolyte interphases in sodium-ion batteries. *Angew. Chem., Int. Ed.* **60**, 4855–4863 (2021).
22. Jin, Y. et al. Low-solvation electrolytes for high-voltage sodium-ion batteries. *Nat. Energy* **7**, 718–725 (2022).
23. Tao, L. et al. Reversible switch in charge storage enabled by selective ion transport in solid electrolyte interphase. *J. Am. Chem. Soc.* **145**, 16538–16547 (2023).
24. Xia, X. et al. Comparison of the reactivity of NaxC6 and LixC6 with non-aqueous solvents and electrolytes. *Electrochem. Solid-State Lett.* **14**, A130 (2011).
25. Eshetu, G. G. et al. Comprehensive insights into the reactivity of electrolytes based on sodium ions. *ChemSusChem* **9**, 462–471 (2016).
26. Mukai, K. et al. Distinguishing the thermal behavior of Na- and Li-intercalated hard carbons via differential scanning calorimetry. *Electrochem. Commun.* **88**, 101–104 (2018).
27. Robinson, J. B. et al. Microstructural analysis of the effects of thermal runaway on Li-ion and Na-ion battery electrodes. *J. Electrochem. Energy Convers. Storage* **15**, 011010 (2018).
28. Seh, Z. W. et al. A highly reversible room-temperature sodium metal anode. *ACS Cent. Sci.* **1**, 449–455 (2015).
29. Qin, B. et al. Sodium hydride inspired the clarification of the ether-carbonate solvent disparity in sodium metal anodes. *Energy Storage Mater.* **61**, 102891 (2023).

30. Li, C. et al. Nonaqueous liquid electrolytes for sodium-ion batteries: fundamentals, progress and perspectives. *Adv. Energy Mater.* **13**, 2301758 (2023).
31. Chen, X. et al. An overall understanding of sodium storage behaviors in hard carbons by an "adsorption-intercalation/filling" hybrid mechanism. *Adv. Energy Mater.* **12**, 2200886 (2022).
32. Yang, Y. et al. Boosting the development of hard carbon for sodium-ion batteries: strategies to optimize the initial Coulombic efficiency. *Adv. Funct. Mater.* **34**, 2302277 (2024).
33. Iglesias, L. K. et al. Revealing the sodium storage mechanisms in hard carbon pores. *Adv. Energy Mater.* **13**, 2302171 (2023).
34. Yuan, M. et al. Sodium storage mechanism of nongraphitic carbons: a general model and the function of accessible closed pores. *Chem. Mater.* **34**, 3489–3500 (2022).
35. Chen, D. et al. Hard carbon for sodium storage: mechanism and optimization strategies toward commercialization. *Energy Environ. Sci.* **14**, 2244–2262 (2021).
36. Hedman, J. et al. Fiber optic sensors for detection of sodium plating in sodium-ion batteries. *ACS Appl. Energy Mater.* **5**, 6219–6227 (2022).
37. Nguyen, L. H. B. et al. First 18650-format Na-ion cells aging investigation: a degradation mechanism study. *J. Power Sources* **529**, 231253 (2022).
38. Vijayakumar, V. et al. In situ polymerization process: an essential design tool for lithium polymer batteries. *Energy Environ. Sci.* **14**, 2708–2788 (2021).
39. Cho, Y. et al. Gel/solid polymer electrolytes characterized by in situ gelation or polymerization for electrochemical energy systems. *Adv. Mater.* **31**, 1804909 (2019).
40. Meng, Y. et al. Designing phosphazene-derivative electrolyte matrices to enable high-voltage lithium metal batteries for extreme working conditions. *Nat. Energy* **8**, 1023–1033 (2023).
41. Zhang, S. et al. In situ-polymerized lithium salt as a polymer electrolyte for high-safety lithium metal batteries. *Energy Environ. Sci.* **16**, 2591–2602 (2023).
42. Zhang, S. et al. Great challenges and new paradigm of the in situ polymerization technology inside lithium batteries. *Adv. Funct. Mater.* **34**, 2314063 (2024).
43. Qiao, L. et al. Review-polymer electrolytes for sodium batteries. *J. Electrochem. Soc.* **167**, 070534 (2020).
44. Yin, H. et al. Recent advances and perspectives on the polymer electrolytes for sodium/potassium-ion batteries. *Small* **17**, 2006627 (2021).
45. Gebert, F. et al. Polymer electrolytes for sodium-ion batteries. *Energy Storage Mater.* **36**, 10–30 (2021).
46. Pan, J. et al. Gel polymer electrolytes design for Na-ion batteries. *Small Methods* **6**, 2201032 (2022).
47. Zheng, J. et al. Progress in gel polymer electrolytes for sodium-ion batteries. *Energy Environ. Mater.* **6**, e12422 (2023).
48. Tian, Z. et al. Electrolyte solvation structure design for sodium ion batteries. *Adv. Sci.* **9**, 2201207 (2022).
49. Zhou, Y. et al. Approaching practically accessible and environmentally adaptive sodium metal batteries with high loading cathodes through in situ interlock interface. *Adv. Funct. Mater.* **32**, 2111314 (2022).
50. Peng, B. et al. Recent progress in the emerging modification strategies for layered oxide cathodes toward practicable sodium ion batteries. *Adv. Energy Mater.* **13**, 2300334 (2023).
51. Zheng, J. et al. Phosphate-based gel polymer electrolyte enabling remarkably long cycling stable sodium storage in a wide-operating-temperature. *Chem. Eng. J.* **465**, 142796 (2023).
52. Zhou, Q. et al. A temperature-responsive electrolyte endowing superior safety characteristic of lithium metal batteries. *Adv. Energy Mater.* **10**, 1903441 (2020).
53. Dong, T. et al. A smart polymer electrolyte coordinates the trade-off between thermal safety and energy density of lithium batteries. *Energy Storage Mater.* **58**, 123–131 (2023).
54. Zhang, J. et al. Smart deep eutectic electrolyte enabling thermally induced shutdown toward high-safety lithium metal batteries. *Adv. Energy Mater.* **13**, 2202529 (2023).
55. Schmiegel, J.-P. et al. Novel in situ gas formation analysis technique using a multilayer pouch bag lithium ion cell equipped with gas sampling port. *J. Electrochem. Soc.* **167**, 060516 (2020).
56. Xu, H. et al. Roll-to-roll prelithiation of Sn foil anode suppresses gassing and enables stable full-cell cycling of lithium ion batteries. *Energy Environ. Sci.* **12**, 2991–3000 (2019).
57. Wang, H. et al. In situ plastic-crystal-coated cathode toward high-performance Na-ion batteries. *ACS Energy Lett.* **8**, 1434–1444 (2023).
58. Liu, X. et al. Suppression of interphase dissolution via solvent molecule tuning for sodium metal batteries. *Adv. Mater.* **35**, 2304256 (2023).
59. Zhou, X. et al. Anion receptor weakens ClO_4^- solvation for high-temperature sodium-ion batteries. *Adv. Funct. Mater.* **34**, 2302281 (2024).
60. Zhong, S. et al. Molecular engineering on solvation structure of carbonate electrolyte toward durable sodium metal battery at −40 °C. *Angew. Chem., Int. Ed.* **62**, e202301169 (2023).
61. Li, J. et al. Weakly coordinating diluent modulated solvation chemistry for high-performance sodium metal batteries. *Angew. Chem. Int. Ed.* **63**, e202400406 (2024).
62. Sun, L. et al. Unraveling and suppressing the voltage decay of high-capacity cathode materials for sodium-ion batteries. *Energy Environ. Sci.* **17**, 210–218 (2024).
63. Pellegrin, E. et al. Soft X-ray magnetic circular dichroism study of the colossal magnetoresistance compound $La_{1-x}Sr_xMnO_3$. *J. Electron Spectrosc. Relat. Phenom.* **86**, 115–118 (1997).
64. Vasiliev, A. N. et al. Valence states and metamagnetic phase transition in partially B-site-disordered perovskite Eu $Mn_{0.5}Co_{0.5}O_3$. *Phys. Rev. B* **77**, 104442 (2008).
65. Hollmann, N. et al. Local symmetry and magnetic anisotropy in multiferroic $MnWO_4$ and antiferromagnetic $CoWO_4$ studied by soft x-ray absorption spectroscopy. *Phys. Rev. B* **82**, 184429 (2010).
66. Yin, Y. et al. $LaMn_3Ni_2Mn_2O_{12}$: an A- and B-site ordered quadruple Perovskite with A-site tuning orthogonal spin ordering. *Chem. Mater.* **28**, 8988–8996 (2016).
67. Wu, H. et al. Orbital order in $La_{0.5}Sr_{1.5}MnO_4$: beyond a common local Jahn-Teller picture. *Phys. Rev. B* **84**, 155126 (2011).
68. Zhong, X. et al. Boosting oxygen reduction activity and enhancing stability through structural transformation of layered lithium manganese oxide. *Nat. Commun.* **12**, 3136 (2021).
69. Nemrava, S. et al. Three oxidation states of manganese in the barium hexaferrite $BaFe_{12-x}Mn_xO_{19}$. *Inorg. Chem.* **56**, 3861–3866 (2017).
70. Liu, H. et al. Insight into the role of metal–oxygen bond and O 2p hole in high-voltage cathode $LiNi_xMn_{2-x}O_4$. *J. Phys. Chem. C.* **121**, 16079–16087 (2017).
71. Amorese, A. et al. Selective orbital imaging of excited states with X-ray spectroscopy: the example of α -MnS. *Phys. Rev. X* **11**, 011002 (2021).
72. Hou, J. et al. Unlocking fast and reversible sodium intercalation in NASICON $Na_4MnV(PO_4)_3$ by fluorine substitution. *Energy Storage Mater.* **42**, 307–316 (2021).
73. Kozakiewicz, J. et al. New family of functionalized crosslinkers for heat-curable polyurethane systems—a preliminary study. *Prog. Org. Coat.* **72**, 120–130 (2011).
74. Wang, R. et al. Electrochemical analysis graphite/electrolyte interface in lithium-ion batteries: p-Toluenesulfonyl isocyanate as electrolyte additive. *Nano Energy* **34**, 131–140 (2017).

75. Hu, P. et al. Fatigue-free and skin-like supramolecular ion-conductive elastomeric interphases for stable lithium metal batteries. *ACS Nano* **17**, 16239–16251 (2023).
76. Guo, X. et al. Interface-compatible gel-polymer electrolyte enabled by NaF-solubility-regulation toward all-climate solid-state sodium batteries. *Angew. Chem., Int. Ed.* **63**, e202402245 (2024).
77. Sun, H. et al. The COMPASS force field: parameterization and validation for phosphazenes. *Comput. Theor. Polym. Sci.* **8**, 229–246 (1998).
78. Sun, H. COMPASS: an ab initio force-field optimized for condensed-phase applications–overview with details on alkane and benzene compounds. *J. Phys. Chem. B* **102**, 7338–7364 (1998).
79. Borodin, O. et al. Competitive lithium solvation of linear and cyclic carbonates from quantum chemistry. *Phys. Chem. Chem. Phys.* **18**, 164–175 (2016).

Acknowledgements

This work was supported by the National Key R&D Program of China (2023YFB2406200), the National Natural Science Foundation of China (22102206, U22A20440, 52403281), the Postdoctoral Fellowship Program of CPSF (GZC20232803), and the Natural Science Foundation of Shandong Provincial (ZR2024YQ008, ZR2024QE095, ZR2024QB020). We acknowledge support from the Max Planck-POSTECH-Hsinchu Center for Complex Phase Materials.

Author contributions

G.C., G.X., H.Z., and T.D. conceived and designed this work. L.D. performed the experiments and wrote the manuscript. C.S. synthesized the polymer materials. L.H., X.Z., and J.L. proposed methods for analyzing battery safety characteristics. S.D., C.L., J.J., and J.Z. provided constructive suggestions and made revision to the manuscript., S.Z., B.X., and J.W. conducted the DSC and XPS tests. J.M., Z.H., Y.Z., F.C., C.K., and C.C. contributed to the XAS measurement. F.S., A.H., and I.M. performed the SXCT measurement.

Competing interests

The authors declare no competing interests.

Additional information

Supplementary information The online version contains supplementary material available at https://doi.org/10.1038/s41467-025-57964-7.

Correspondence and requests for materials should be addressed to Gaojie Xu, Huanrui Zhang, Tiantian Dong or Guanglei Cui.

Peer review information *Nature Communications* thanks Dong-Joo Yoo, and the other, anonymous, reviewer(s) for their contribution to the peer review of this work. A peer review file is available.